The Astrophysical Journal, 927:176 (10pp), 2022 March 10 https://doi.org/10.3847/1538-4357/ac503d
© 2022. The Author(s). Published by the American Astronomical Society.
OPEN ACCESS

The Farthest Quasar Mini-Broad Absorption Line Outflow from Its Central Source: Very Large Telescope/UVES Observation of SDSS J0242+0049

Doyee Byun[1], Nahum Arav[1], and Patrick B. Hall[2]
[1] Department of Physics, Virginia Tech, Blacksburg, VA 24061, USA
[2] Department of Physics and Astronomy, York University, Toronto, ON, M3J 1P3, Canada
Received 2021 October 8; revised 2021 December 22; accepted 2022 January 28; published 2022 March 14

Abstract

We analyze Very Large Telescope/UVES observations of the quasar SDSS J024221.87+004912.6. We identify four absorption outflow systems: a C IV broad absorption line (BAL) at $v \approx -18{,}000$ km s^{-1} and three narrower low-ionization systems with centroid velocities ranging from –1200 to –3500 km s^{-1}. These outflows show similar physical attributes to the [O III] outflows studied by Liu et al. (2013). We find that two of the systems are energetic enough to contribute to active galactic nucleus feedback, with one system reaching above 5% of the quasar's Eddington luminosity. We also find that this system is at a distance of 67 kpc away from the quasar, the farthest detected mini-BAL absorption outflow from its central source to date. In addition, we examine the time-variability of the BAL and find that its velocity monotonically increases, while the trough itself becomes shallower over time.

Unified Astronomy Thesaurus concepts: Active galactic nuclei (16); Quasars (1319); Quasar absorption line spectroscopy (1317); Galaxies (573); AGN host galaxies (2017)

1. Introduction

Quasar absorption outflows are seen in a large fraction of quasar spectra ($\lesssim$40%), often detected via blueshifted absorption troughs in the rest frame of quasars (Hewett & Foltz 2003; Dai et al. 2008; Knigge et al. 2008). These outflows are often mentioned as likely candidates for producing active galactic nucleus (AGN) feedback (e.g., Silk & Rees 1998; Scannapieco & Oh 2004; Ciotti et al. 2009; Yuan et al. 2018; Vayner et al. 2021). According to theoretical models, outflow systems require a kinetic luminosity ($\dot{E}_k$) of at least ∼0.5% (Hopkins & Elvis 2010) or ∼5% (Scannapieco & Oh 2004) of the quasar's Eddington luminosity ($L_{\rm Edd}$) to contribute to AGN feedback. Outflow systems that fit these criteria have been found (e.g., Moe et al. 2009; Arav et al. 2013; Chamberlain et al. 2015; Xu et al. 2019, 2020a; Miller et al. 2020a; Xu et al. 2020b; Miller et al. 2020b; Arav et al. 2020).

The kinetic luminosity of a quasar's outflow system is dependent on its distance from its central source (R), which we can find by measuring both the electron number density (n_e) and ionization parameter ($U_{\rm H}$) (Borguet et al. 2012a). Our group and others have used this method to find the distances of outflow systems in the past (de Kool et al. 2001; Hamann et al. 2001; de Kool et al. 2002; Gabel et al. 2005; Borguet et al. 2012a; Xu et al. 2018; Miller et al. 2020a; Arav et al. 2020). Using the ratios between excited and resonance state column densities of ionized species ($N_{\rm ion}$) can lead us to a value of n_e (Arav et al. 2018). This paper presents one such determination of the R and $\dot{E}_k$ values of three outflow components found in the Very Large Telescope (VLT)/UVES spectrum of SDSS J024221.87+004912.6 (hereafter J0242+0049).

The analysis of J0242+0049 shown in this paper is based on data from the VLT/UVES Spectral Quasar Absorption Database (SQUAD) published by Murphy et al. (2019), which contains the spectra of 475 quasars. Analysis of more SQUAD objects will be conducted in the future.

The UVES data of J0242+0049 are from program 075.B-0190 (A), which Hall et al. (2007) used to identify a high-velocity C IV broad absorption line (BAL) at $z \approx 1.88$ ($v \approx -18{,}000$ km s^{-1}), as well as two mini-BAL outflows and one narrow absorption line (NAL) outflow at lower velocities; we have identified all four independently. Comparing the UVES spectrum to SDSS spectra from previous epochs, Hall et al. (2007) have identified a shift in the velocity of the high-velocity BAL, which could potentially be explained by acceleration. They have also found potential line locking in the Si IV absorption doublets of the two lower-velocity mini-BAL systems. In addition to the analysis of the UVES data, we conduct a follow-up to their observation of the velocity shift using SDSS observation data from more recent epochs.

This paper is structured as follows. Section 2 discusses the observation of J0242+0049, as well as the data acquisition process. In Section 3, we present the ionic column density measurements and the process of finding n_e and $U_{\rm H}$. Section 4 shows the results of the analysis, including the energetics parameters of the outflow systems. We also show observations of the high-velocity BAL from recent SDSS epochs. Section 5 provides a discussion of the results, and Section 6 summarizes and concludes the paper. For this analysis, we adopt a cosmology of $h = 0.696$, $\Omega_m = 0.286$, and $\Omega_\Lambda = 0.714$ (Bennett et al. 2014) and use the Python astronomy package Astropy (Astropy Collaboration et al. 2013, 2018) for cosmological calculations.

2. Observation, Data Acquisition, and Line Identification

The quasar J0242+0049 (J2000: R.A. = 02:42:22, decl. = +00:49:12.6; $z = 2.06$) (Pâris et al. 2018) was observed in 2005 September 5, with the VLT/UVES as part of program 075.B-0190(A), with resolution $R \simeq 40{,}000$ and wavelength coverage from 3291 to 9300 Å (Hall et al. 2007). The systemic redshift $z = 2.06$ given by Murphy et al. (2019) is consistent with the value we find based on the Mg II emission line in the SDSS spectrum of the MJD = 57758 epoch. The spectral data

Original content from this work may be used under the terms of the Creative Commons Attribution 4.0 licence. Any further distribution of this work must maintain attribution to the author(s) and the title of the work, journal citation and DOI.

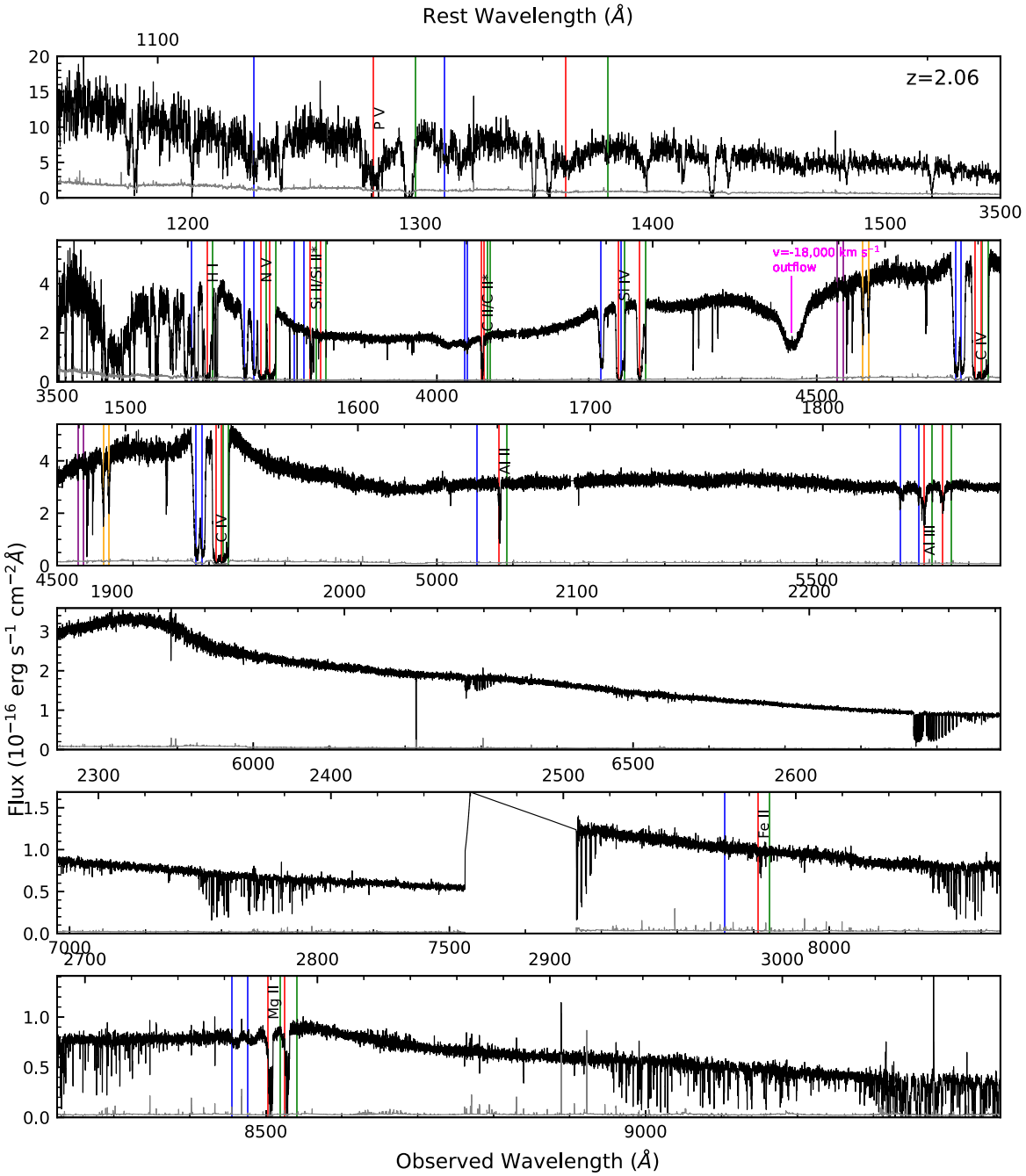

Figure 1. Normalized flux of J0242+0049 multiplied by the emission model by Murphy et al. (2019), based on the SQUAD data set. The flux has been scaled to match the BOSS spectrum from the epoch of MJD = 57758 (2017 January 5) at the observed wavelength $\lambda = 6500$ Å. The black curve represents the flux, and the gray shows the error in flux. The green, red, and blue vertical lines mark absorption troughs of outflow systems S1, S2, and S3, respectively, while the S4 C IV BAL is labeled in magenta. Systems A and B are marked in orange and purple, respectively. Note that the absorption troughs for S1 are significantly narrower when compared to those of S2 and S3.

was reduced and normalized by its continuum and emission by Murphy et al. (2019) as part of their SQUAD database. Broad and narrow absorption lines have been found in the spectrum of J0242+0049 by Hall et al. (2007), which we identify here as NAL S1 at $-1200\,\mathrm{km\,s^{-1}}$ (Lyα FWHM $= 240\,\mathrm{km\,s^{-1}}$), mini-BAL S2 at $-1800\,\mathrm{km\,s^{-1}}$ (N V FWHM $= 900\,\mathrm{km\,s^{-1}}$), mini-BAL S3 at $-3500\,\mathrm{km\,s^{-1}}$ (N V FWHM $= 720\,\mathrm{km\,s^{-1}}$), and the aforementioned BAL S4 at $-18{,}000\,\mathrm{km\,s^{-1}}$, as shown in the full spectrum in Figure 1. Following Weymann et al. (1991), a BAL is a continuous absorption feature below 0.9 normalized intensity over $2000\,\mathrm{km\,s^{-1}}$, a mini-BAL is the same but between 500 and $2000\,\mathrm{km\,s^{-1}}$ (Hamann & Sabra 2004), and an NAL is an absorption feature with width below $500\,\mathrm{km\,s^{-1}}$. We measure the width of S4 at 0.9 normalized intensity to be $2200\,\mathrm{km\,s^{-1}}$, which is above the threshold of a BAL, with a balnicity index, as defined by Weymann et al. (1991), of $660\,\mathrm{km\,s^{-1}}$. Chen et al. (2021) have identified four C IV absorption systems, two of which coincide with systems S3 and S4. We label the other two as systems A and B and show them in Figure 1. The focus of this paper is on the four systems S1, S2, S3, and S4. We do not discuss systems A and B because they only show absorption in C IV, which does not lend itself to further analysis.

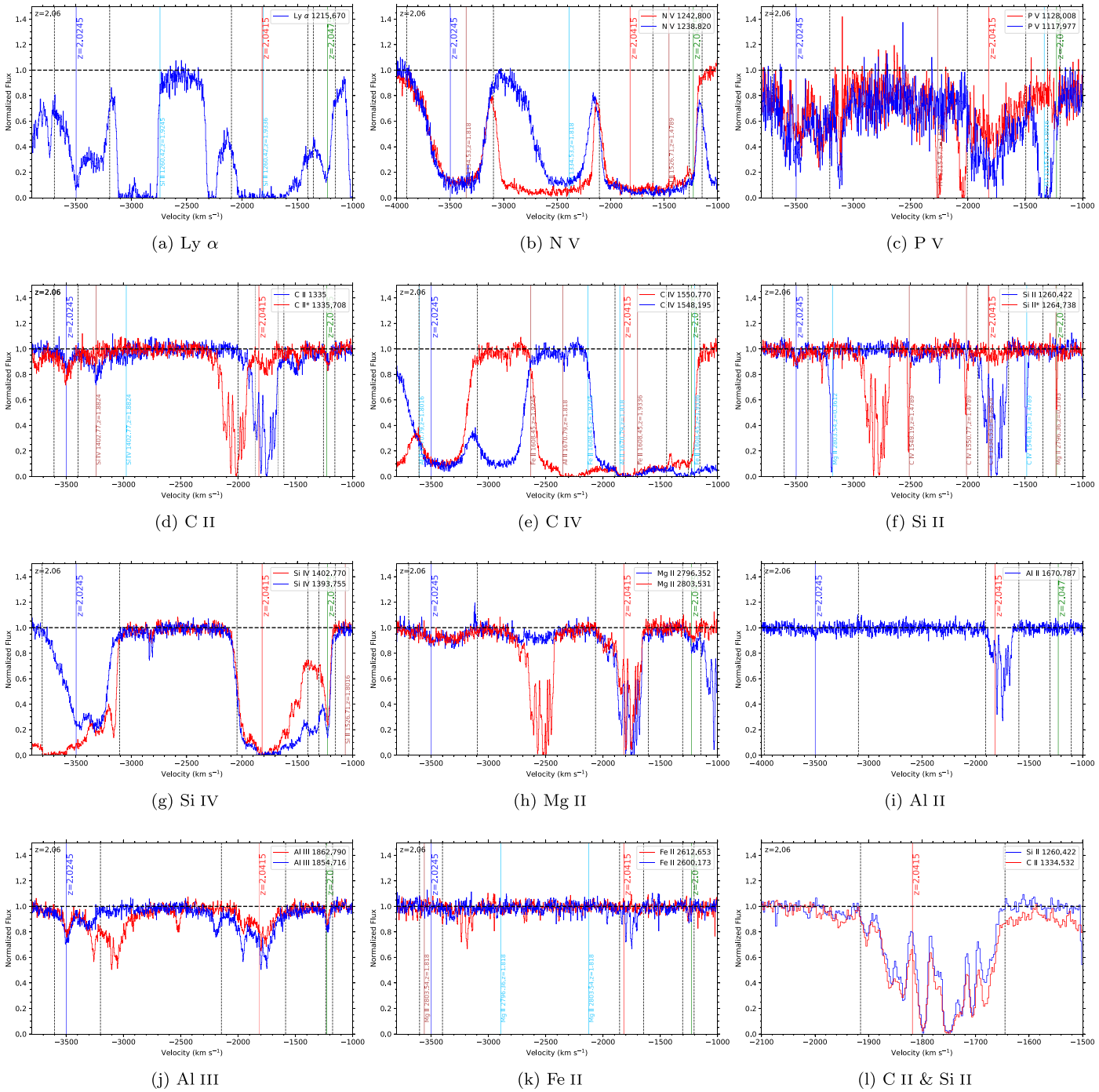

Figure 2. Normalized spectrum plotted in velocity space for each ion in the absorption systems. The green, red, and blue vertical lines represent the velocity of systems S1, S2, and S3, respectively. The dotted vertical lines show the integration ranges used for the calculation of the ionic column densities. The horizontal dashed line represents the continuum level. Intervening absorption systems that contaminate the blue spectra are marked with cyan vertical lines, while intervening systems contaminating the red spectra are marked with brown vertical lines. Note in plot (f) that the S1 integration range for Si II 1265 Å is contaminated with the Mg II 2796 Å absorption of the $z = 0.3783$ intervening system. Plot (l) shows the structure of the S2 absorption trough of Si II and C II, on a narrower velocity scale.

The outflows show absorption from low-ionization species such as Si II, C II, and Fe II, as well as lines of Ly α, C IV, N V, P V, Mg II, Al II, and Al III. For the purpose of measuring the ionic column densities, we convert the normalized spectrum data from wavelength to velocity space via the systemic redshift of the quasar, as shown in Figure 2. Note that S2 appears to be composed of at least seven subcomponents, as seen in plot (l) of Figure 2. The components are blended in the absorption troughs of C IV and Si IV, and due to the shallowness of the C II* troughs, it is impossible to decompose it into the different subcomponents. For this reason, they are treated as a singular absorption system for the sake of analysis in this paper.

For the velocity-shift analysis, SDSS spectra from MJD = 52177, 52199, 55455, and 57758 were retrieved and corrected for galactic extinction with $E(B-V) = 0.0269$ (Schlafly & Finkbeiner 2011). The spectra from both the BOSS and SDSS spectrographs have spectral resolutions of $R \approx 2000$

Table 1
SDSS Spectra Information

Epoch in MJD	Spectrograph	Plate	Fiber	Observed Date	Wavelength Coverage (Å)
52177	SDSS	707	332	2001 Sep 25	3824–9215
52199	SDSS	706	617	2001 Oct 17	3820–9202
55455	BOSS	4240	754	2010 Sep 16	3590–10382
57758	BOSS	9381	79	2017 Jan 5	3573–10334

(Schneider et al. 2010; Smee et al. 2013; Pâris et al. 2018). More details on the SDSS spectra can be found in Table 1.

3. Analysis

3.1. Ionic Column Density

To find the physical characteristics of the outflow systems, we first find the column densities of the observed ions ($N_{\rm ion}$). The simplest method for measuring column densities is by assuming the apparent optical depth (AOD) of a uniformly covered homogeneous source, as demonstrated by Savage & Sembach (1991). When calculating column density under this assumption, we first assume the relation between intensity and optical depth as follows (see Equation (1) of Savage & Sembach 1991):

$$I(\lambda) = I_0(\lambda)e^{-\tau(\lambda)}, \quad (1)$$

where $I(\lambda)$ is the intensity, $I_0(\lambda)$ is the intensity without absorption, and $\tau(\lambda)$ is the optical depth as a function of wavelength. When writing optical depth as a function of outflow velocity, it has a relation with column density $N(v)$ of (see Equation (8) of Savage & Sembach 1991):

$$\tau(v) = \frac{\pi e^2}{m_e c} f\lambda N(v), \quad (2)$$

where m_e is the mass of an electron, e is the elementary charge, and f and λ are the oscillator strength and wavelength of the transition line, respectively. Finding $N(v)$ and integrating it over the velocity range of the absorption trough yields the column density based on the AOD assumption. The AOD method is used to find lower limits of $N_{\rm ion}$ for singlets or contaminated doublets, or upper limits when there are no discernible absorption troughs.

When there are multiple lines of the same ion and energy state, we can use the partial covering (PC) method, which assumes a homogeneous source partially covered by the outflow (Barlow et al. 1997; Arav et al. 1999a, 1999b) and solves for a velocity-dependent covering factor (de Kool et al. 2002; Arav et al. 2005), to improve our measurements by taking phenomena such as nonblack saturation into account (Edmonds et al. 2011; Borguet et al. 2012). When calculating the PC-based column density of an ion with a doublet of transition lines, we find the covering fraction $C(v)$ via the following relations (see Equations (2) and (3) of Arav et al. 2005):

$$I_R(v) - [1 - C(v)] = C(v)e^{-\tau(v)}, \quad (3)$$

$$I_B(v) - [1 - C(v)] = C(v)e^{-2\tau(v)}, \quad (4)$$

where $I_R(v)$ and $I_B(v)$ are the normalized intensities of the red and blue absorption features, respectively, and $\tau(v)$ is the optical depth of the red component.

We choose integration ranges that cover visible absorption in the data, as can be seen in Figure 2, while minimizing the effects of blending and contamination. For instance, for Si IV, we use the blue line for S3 and the red line for S2. Si II* of S1 shows contamination due to an intervening absorption feature, so we use the measured column density as an upper limit for the sake of our analysis. The C IV of S2 is heavily blended between the red and blue features, so we choose a velocity range in which the blue and red spectra do not overlap with each other in order to find a lower limit of the column density.

Attempting a Gaussian fit of the C IV absorption of S2 yields a poor fit due to the saturation of the trough. Calculating the column density based on the fit results in a lower limit of $2400 \times 10^{12}\,{\rm cm}^{-2}$, compared to the measured lower limit of $3900 \times 10^{12}\,{\rm cm}^{-2}$. This difference does not affect the solution of the hydrogen column density and photoionization parameter as described in Section 3.2.

The measured column density values can be found in Table 2. Note that most adopted values in Table 2 are upper or lower limits. The errors in the column densities are propagated from the errors in the normalized flux from the data, binned along with the data into segments of $\Delta v = 10\,{\rm km\,s}^{-1}$ for numerical integration. A 20% error is added in quadrature for the column density values adopted for photoionization analysis (see the last column of Table 2) to take into account the uncertainty in the modeled continuum level (Xu et al. 2018).

3.2. Photoionization Analysis

We use a grid of photoionization models created using the spectral synthesis code Cloudy (version c17.00; Ferland et al. 2017), in order to find the hydrogen column density ($N_{\rm H}$) and ionization parameter ($U_{\rm H}$) that best fit the measured ionic column densities, following the method of previous works (e.g., Miller et al. 2018; Xu et al. 2019; Miller et al. 2020a).

We use Cloudy to create a grid of simulated models that correspond to different $N_{\rm H}$ and $U_{\rm H}$ values, assuming solar metallicity, and the spectral energy distribution (SED) of quasar HE 0238–1904 (hereafter HE0238; Arav et al. 2013). The $N_{\rm H}$ and $U_{\rm H}$ parameters determine the ionic column densities of each model, which we compare with the measured column densities shown in Table 2. For S2, including the lower bound of the Fe II column density in the analysis introduced an $N_{\rm H}$ and $U_{\rm H}$ solution that was contradictory to the constraints from the other ions. We suspect that this is because the Fe abundance of the system does not match solar metallicity ($Z_\odot$), requiring a metallicity of $\sim$10 $Z_\odot$. This is in approximate agreement with the highest outflow metallicity found by Gabel et al. (2006; $Z \approx 5\ Z_\odot$). For this reason, we model our solution using the other ions but excluding Fe II. The $\log N_{\rm H}$ and $\log U_{\rm H}$ values from this analysis are shown in Table 3, as well as in Figure 3.

Table 2
J0242+0049 Outflow Ionic Column Densities

Troughs	AOD	PC	Adopted
S1, $v = -1200$ km s^{-1}			
H I	$177.0^{+1.9}_{-1.8}$		$>180_{-40}$
N V	467^{+5}_{-5}		$>470_{-90}$
P V	56^{+4}_{-4}		$>50_{-10}$
C II total	26^{+2}_{-2}		$>26_{-5}$
C II 1335	$10.8^{+1.5}_{-1.2}$		
C II* 1336	$14.7^{+1.5}_{-1.3}$		
C IV	350^{+5}_{-4}		$>350_{-70}$
Si II total	$5.5^{+0.3}_{-0.4}$		$<5.5^{+1.2}$
Si II 1260	$1.3^{+0.3}_{-0.2}$		$<1.3^{+0.4}$
Si II* 1265	$2.8^{+0.2}_{-0.2}$		$<2.8^{+0.6}$
Si IV	$92.6^{+1.0}_{-1.0}$		$>90_{-20}$
Mg II	$2.7^{+0.3}_{-0.3}$		$>2.7_{-0.6}$
Al II	$0.3^{+0.09}_{-0.08}$		$<0.3^{+0.1}$
Al III	$3.3^{+0.3}_{-0.3}$	$4.9^{+0.8}_{-0.5}$	$4.9^{+1.3}_{-1.1}$
Fe II	$1.9^{+0.4}_{-0.3}$		$<1.9^{+0.5}$
S2, $v = -1800$ km s^{-1}			
H I	1680^{+180}_{-10}		$>1680_{-340}$
N V	4620^{+30}_{-30}		$>4620_{-920}$
P V	450^{+10}_{-10}		$>450_{-90}$
C II total	740^{+90}_{-10}		$>740_{-150}$
C II 1335	690^{+90}_{-10}		
C II* 1336	50^{+2}_{-2}		
C IV	3910^{+330}_{-20}		$>3910_{-780}$
Si II total			$>80_{-20}$
Si II 1260	$77.6^{+1.3}_{-1.1}$		$>80_{-20}$
Si II* 1265	$2.9^{+0.3}_{-0.3}$		$<3^{+0.7}$
Si IV	1410^{+100}_{-10}		$>1410_{-280}$
Mg II	$84^{+1.0}_{-0.9}$	$90.7^{+1.0}_{-1.0}$	90^{+20}_{-20}
Al II	$10.3^{+0.2}_{-0.1}$		$>10_{-2}$
Al III	$48.4^{+0.9}_{-0.9}$	$55.6^{+0.9}_{-0.8}$	55^{+10}_{-10}
Fe II total			$>12_{-2.5}$
Fe II 2600	$12.2^{+0.5}_{-0.5}$		$>12_{-2.5}$
Fe II* 2612	$1.0^{+0.5}_{-0.5}$		$<1.0^{+0.5}$
S3, $v = -3500$ km s^{-1}			
H I	$417.7^{+3.7}_{-3.4}$		$>420_{-80}$
N V	3780^{+20}_{-20}		$>3780_{-760}$
P V	390^{+10}_{-10}		$>390_{-80}$
C II total	$94.2^{+3.5}_{-3.3}$		$>90_{-20}$
C II 1335	$32^{+2.4}_{-2.2}$		
C II* 1336	$62.1^{+2.5}_{-2.5}$		
C IV	2180^{+10}_{-10}		$>2180_{-440}$
Si II total	$5.1^{+0.4}_{-0.3}$		$>5.1_{-1.1}$
Si II 1260	$2.5^{+0.3}_{-0.3}$		
Si II* 1265	$2.6^{+0.2}_{-0.2}$		
Si IV	$285.8^{+1.5}_{-1.4}$		$>290_{-60}$
Mg II	$17.9^{+0.6}_{-0.6}$		$>18_{-4}$
Al II	$2^{+0.2}_{-0.2}$		$<2^{+0.4}$
Al III	$19.7^{+0.4}_{-0.4}$		$>20_{-4}$
Fe II total	$6.7^{+0.7}_{-0.9}$		$<6.7^{+1.5}$
Fe II 2600	$2.2^{+0.4}_{-0.5}$		
Fe II* 2612	$4.5^{+0.6}_{-0.7}$		

Notes. Units are in 10^{12} cm^{-2}. Values have been calculated by numerical integration over bins with width $\Delta v = 10$ km s^{-1}. Note that most of the adopted values are upper or lower limits.

3.3. Electron Number Density

The electron number density and, by extension, the distance of the outflow systems from the central source, can be found by determining the abundance ratios, measured via column densities, between excited and resonance states of low-ionization species (Moe et al. 2009). We use the CHIANTI 9.0.1 Database (Dere et al. 1997, 2019) to model the relationship between the ratio of excited and resonance state ion abundances, and the electron number density, based on collisional excitation. We overlay this relation with the ratios based on the measured column densities, as shown in Figure 4. For this object, we use the ratios N(Si II*)/N(Si II), N(C II*)/N(C II), and N(Fe II*)/N(Fe II), where N(ion) is the column density of a particular ion.

For S3, we have an upper limit given by the C II ratio and a measurement from the Si II ratio, which agree with one another. Our measurements of Fe II are dominated by noise and, as such, are not included in the n_e measurement. Taking the ratio of N(Si II*)/N(Si II), we find that $\log n_e = 3.3^{+0.8}_{-0.4}$ [cm^{-3}]. S2 provides us a measurement from C II and upper limits from Si II and Fe II. From the N(C II*)/N(C II) ratio, we find $\log n_e = 0.25^{+0.2}_{-0.2}$ [cm^{-3}]. S1 only gives us a lower limit from C II, as Si II* is contaminated by an intervening line and cannot give us a reliable ratio between N(Si II*) and N(Si II). Thus, we get a lower limit for the electron number density, $\log n_e > 2.0_{-0.45}$ [cm^{-3}].

4. Results

4.1. Distance and Kinetic Luminosity of the Outflows

In order to find the distance of the outflow systems, we use the definition for the ionization parameter

$$U_{\rm H} \equiv \frac{Q_{\rm H}}{4\pi R^2 n_{\rm H} c}, \quad (5)$$

where $Q_{\rm H}$ is the rate of ionizing photons, R is the distance of the outflow from the central source, and $n_{\rm H}$ is the hydrogen number density, which is estimated as $n_e \approx 1.2 n_{\rm H}$ for highly ionized plasma (Osterbrock & Ferland 2006). Because we have a solution for $U_{\rm H}$ from our photoionization analysis, as well as the n_e for each outflow from the excited to resonance state ratios, we can find R after determining the value of $Q_{\rm H}$. We determined $Q_{\rm H}$ by first scaling the HE0238 SED to match the continuum flux at observed wavelength $\lambda = 6500$ Å from the most recent SDSS observation ($F_\lambda = 1.4^{+0.14}_{-0.14} \times 10^{-16}$ erg s^{-1} cm^{-2} Å^{-1}) and integrating over the scaled SED for energies above 1 Ryd, yielding $Q_{\rm H} = 1.21^{+0.11}_{-0.11} \times 10^{57}$s^{-1}. The corresponding $L_{\rm bol} = 1.93^{+0.18}_{-0.18} \times 10^{47}$ erg s^{-1} is larger than what would be expected from calculating the νL_νat a specific wavelength via the method employed by Allen et al. (2011), as the HE0238 SED shows a large peak at the UV range ($\lambda \approx 1000$ Å; Arav et al. 2013). Applying a bolometric correction appropriate to 1700 Å from Richards et al. (2006) brings the νL_ν reported by Allen et al. (2011) to within 20% of our calculated $L_{\rm bol}$. The resulting outflow distances are shown in Table 3. Note that the distance of S2 (–1800 km s^{-1}, $R = 67^{+55}_{-31}$kpc) is at least an order of magnitude larger than that of S3 (–3500 km s^{-1}, $R = 1.2^{+0.8}_{-0.9}$ kpc) or S1 (–1200 km s^{-1}, $R < 5.4^{+7.3}$ kpc).

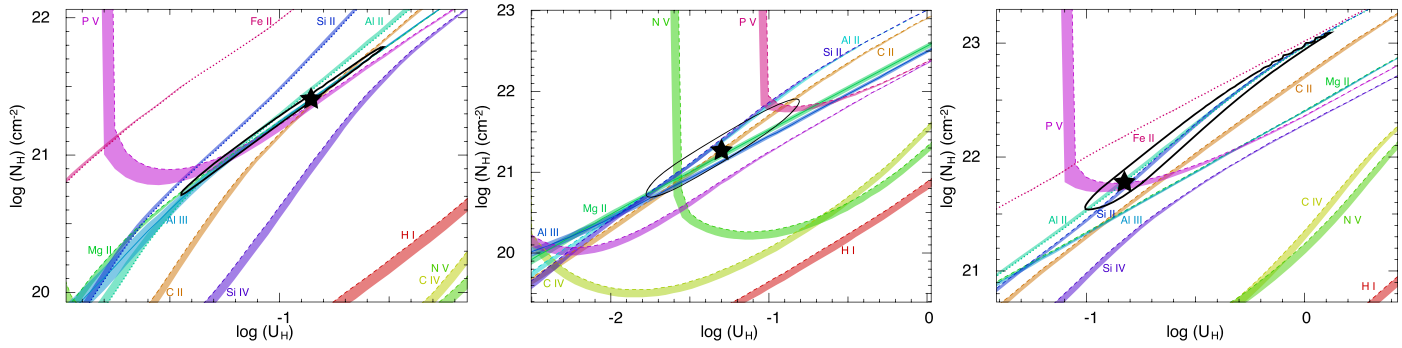

Figure 3. Plots of $\log N_{\rm H}$ vs. $\log U_{\rm H}$ for (a) S1, (b) S2, and (c) S3. The colored lines represent the $N_{\rm H}$ and $U_{\rm H}$ values allowed by the measured column densities of ions. Solid lines show measurements, dashed lines show lower limits, and dotted lines show upper limits. The colored bands attached to the lines represent the uncertainties in the column density measurements. The black stars in the plots show the solution for $N_{\rm H}$ and $U_{\rm H}$ found via χ^2 minimization, and the black ellipses represent the 1σ range for the solutions. For this calculation, the HE0238 SED and solar metallicity are assumed.

Table 3
Physical Properties of the J0242+0049 Outflow Systems

Outflow System	S1 = −1200 km s^{-1}	S2 = −1800 km s^{-1}	S3=−3500 km s^{-1}
$\log(N_{\rm H})$ [cm^{-2}]	$21.41^{+0.38}_{-0.70}$	$21.27^{+0.64}_{-0.58}$	$21.78^{+1.30}_{-0.24}$
$\log(U_{\rm H})$ [dex]	$-0.86^{+0.33}_{-0.59}$	$-1.30^{+0.49}_{-0.48}$	$-0.83^{+0.95}_{-0.18}$
$\log(n_{\rm e})$ [cm^{-3}]	$>2.00_{-0.45}$	$0.25^{+0.20}_{-0.20}$	$3.30^{+0.75}_{-0.40}$
Distance [kpc]	$<5.4^{+7.3}$	67^{+55}_{-31}	$1.2^{+0.8}_{-0.9}$
$\dot{M}$ [$M_\odot$ yr^{-1}]	$<480^{+300}$	6500^{+8900}_{-3400}	700^{+2900}_{-30}
$\dot{M}v$ [10^{36} erg cm^{-1}]	$<3.6^{+2.3}$	74^{+100}_{-39}	$16^{+60}_{-0.7}$
$\log(\dot{E}_K)$ [erg s^{-1}]	$<44.33^{+0.21}$	$45.82^{+0.37}_{-0.32}$	$45.43^{+0.7}_{-0.02}$
$\dot{E}_K/L_{edd}$ [%]	$<0.18^{+0.16}$	$5.5^{+8.8}_{-3.1}$	$2.3^{+9.9}_{-0.8}$

Note. A temperature of 10,000 K is assumed.

Once we have the distance of the outflow, we can find the mass flow rate (Borguet et al. 2012b),

$$\dot{M} \simeq 4\pi\Omega R N_H \mu m_p v, \quad (6)$$

and the kinetic luminosity,

$$\dot{E}_k \simeq \frac{1}{2}\dot{M}v^2, \quad (7)$$

assuming a partially filled shell, where Ω is the global covering factor (fraction of the total solid angle of the quasar that the outflow covers), $\mu = 1.4$ is the mean atomic mass per proton, m_p is the proton mass, and v is outflow velocity. For the global covering factor, we assume $\Omega = 0.2$, the portion of quasars from which C IV BALs are found (Hewett & Foltz 2003). As explained by Dunn et al. (2010), this is a reasonable assumption despite the relative rarity of quasars showing singly ionized absorption troughs such as Si II, due to the likelihood that such quasars are regular BAL quasars seen from specific lines of sight. The resulting kinetic luminosity calculations yield $\log \dot{E}_K$ [erg s^{-1}] $= 45.42^{+1.33}_{-0.64}$, $45.82^{+0.37}_{-0.32}$ for

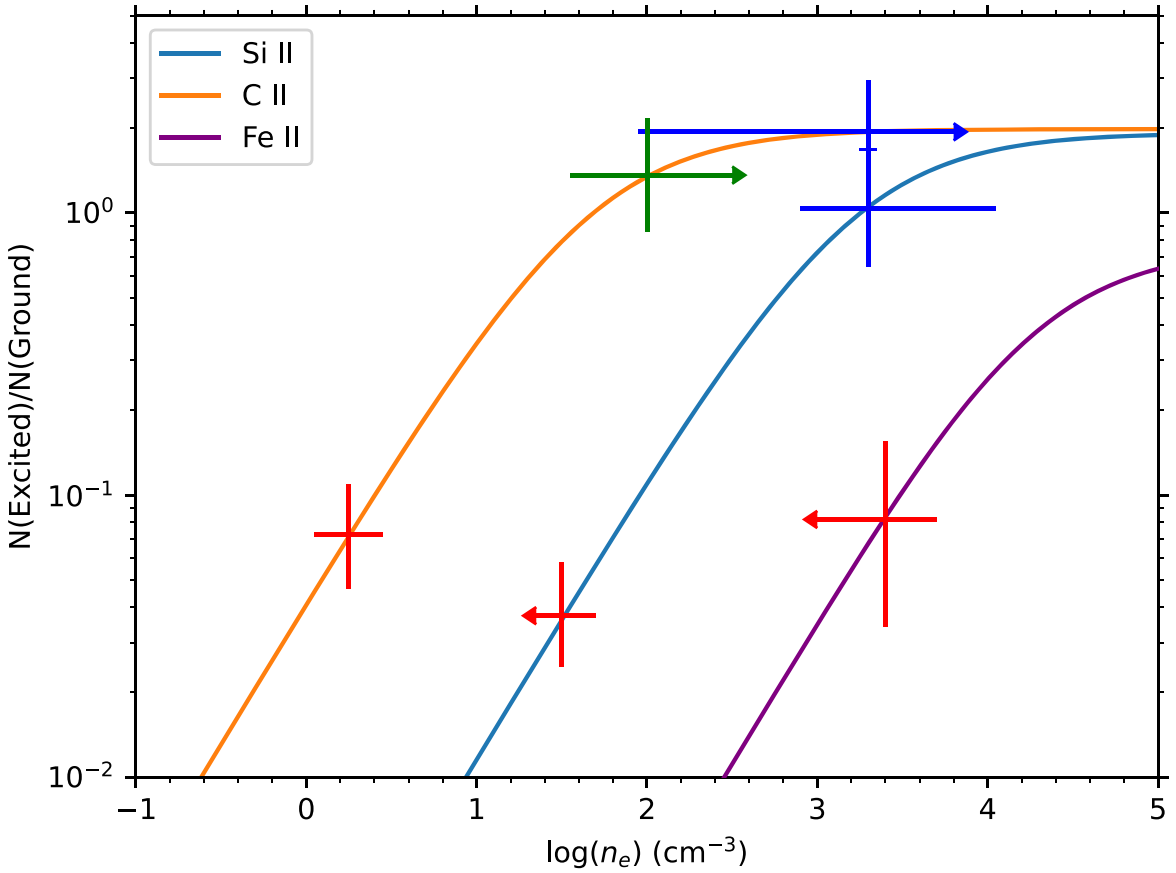

Figure 4. Ratio between excited and resonance state abundances of Si II, C II, and Fe II vs. $\log n_e$. The curves marked Si II, C II, and Fe II are the theoretical ratios modeled with CHIANTI, assuming a temperature of 10,000 K. The crosses on the curves show the ranges of the C II, Si II, and Fe II column density ratios, based on the measured AOD column densities. The green, red, and blue correspond to systems S1, S2, and S3, respectively. Arrows indicate either upper or lower limits in $\log n_e$ depending on the direction of the arrow. The upper limit of the N(Si II*)/N(Si II) ratio for S3 is marked with a tick, as it overlaps with the error bars of the C II ratio of the same system.

S3 and S2, respectively, as well as an upper limit of $\log \dot{E}_K < 44.33^{+0.53}$ for S1. In addition, we calculate the momentum flux ($\dot{M}v$) of each outflow system (see Table 3) and compare it to the single-scattering limit of the quasar $\left(\frac{L_{\rm bol}}{c} = 6.44^{+0.61}_{-0.61} \times 10^{36}\text{erg cm}^{-1}\right)$. The single-scattering limit assumes the scenario in which absorption of photon momentum drives acceleration (Abbott 1982; Arav & Li 1994). The momentum flux of S1 is smaller than the single-scattering limit, while those of S2 and S3 are above the limit. As S2 has a momentum flux an order of magnitude higher than the single-scattering limit, this implies the possibility of a multiple-scattering scenario (Lucy & Abbott 1993).

4.2. Changes in the High-velocity BAL Trough (S4)

Following up on the results reported by Hall et al. (2007), we examine the velocity shift of the C IV BAL of S4. Using two Gaussian profiles, one broad and shallow, and the other narrow and deep, we modeled the absorption in each of the five epochs, as shown in Figure 5. We can see that the centroid velocity of the narrow Gaussian monotonically grows, while the equivalent width becomes smaller from epoch to epoch. Detailed information on the centroid velocities and equivalent widths per epoch can be seen in Table 4.

Assuming acceleration along the line of sight, based on the centroid velocities of the narrow Gaussian, the average acceleration between the observations in 2001 September and 2017 January would be $a = -0.25 \pm 0.13\,\text{cm s}^{-2}$ in the quasar's rest frame, which agrees within error with the acceleration $a = -0.154 \pm 0.025\,\text{cm s}^{-2}$ between 2001 September 1 and 2005 September found by Hall et al. (2007). Due to the shrinking of the trough, we must take into consideration effects other than the line-of-sight acceleration, such as changes in photoionization, as discussed by Xu et al. (2020c).

5. Discussion

5.1. AGN Feedback Contribution of Outflows

As previously mentioned in the introduction, the kinetic luminosity ($\dot{E}_k$) of the outflow systems must be at least ∼0.5% (Hopkins & Elvis 2010) or ∼5% (Scannapieco & Oh 2004) of the source quasar's Eddington luminosity ($L_{\rm Edd}$) to contribute to AGN feedback. In order to find this ratio, we must first find the Eddington luminosity. We compute the mass of the black hole using the Mg II–based mass equation in Bahk et al. (2019), with the FWHM of the Mg II emission feature in the SDSS spectrum. To account for the Fe II emission throughout the spectrum, we use the Fe II template by Tsuzuki et al. (2006) and run a best-fit algorithm to match the features in the spectrum, as done by Woo et al. (2018). This yields a black hole mass of $M_{\rm BH} = 9.7^{+4.9}_{-3.4} \times 10^8\,M_\odot$, corresponding to an Eddington luminosity of $L_{\rm Edd} = 1.2^{+0.6}_{-0.4} \times 10^{47}\text{erg s}^{-1}$. We expect the Fe II emission's effect on the absorption to be small,

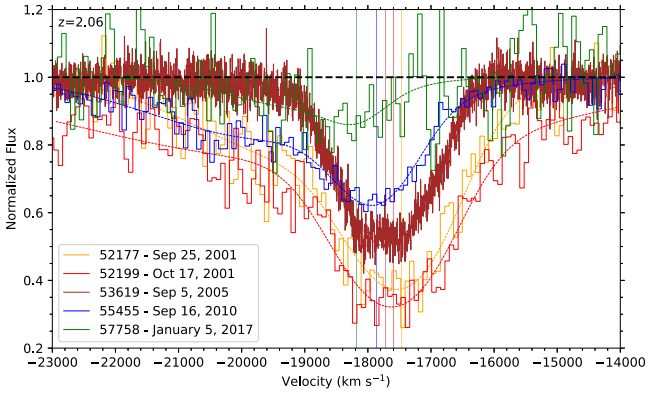

(a)

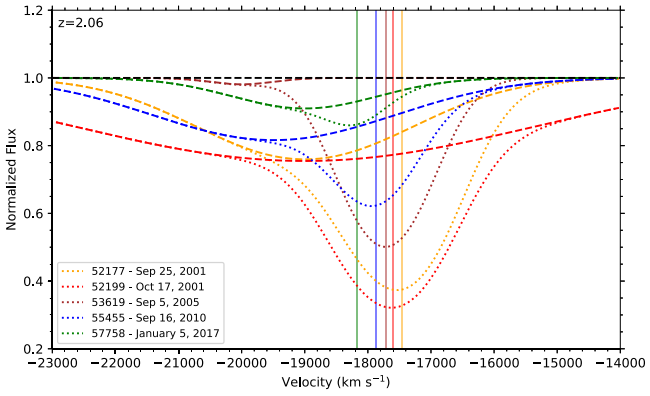

(b)

Figure 5. Normalized flux vs. velocity of the S4 C IV BAL at different epochs. The trough has been modeled by employing a best fit of a profile of two Gaussians, one wide and one narrow. (a) shows Gaussian models of the troughs over the data, while (b) shows the Gaussian models independently. The colored vertical lines mark the centroid velocities at each epoch. Note that the centroid velocity increases through each epoch, while the equivalent width decreases.

as the fitted emission template from Tsuzuki et al. (2006) is <20% of the continuum level of the SDSS spectrum of MJD = 57758, leaving us with column densities that agree with our measured values within error.

Taking the ratio between the kinetic luminosity of each outflow system and the Eddington luminosity of the quasar, we find that S2 and S3 are well above the 0.5% threshold from Hopkins & Elvis (2010) and S2 is above the 5% threshold by Scannapieco & Oh (2004), while S1's kinetic luminosity is below 0.18% of the Eddington luminosity, as seen in Table 3. We can thus conclude that S2 and S3 are energetic enough to contribute to AGN feedback.

Unlike in objects analyzed in other papers (e.g., Xu et al. 2020a; Miller et al. 2020a), we do not have lines from the very-high-ionization phase. Thus, while there may be a very-high-ionization phase, we cannot tell from the information we have.

5.2. Time-variability of Troughs

Following the examination of the S4 C IV BAL at different epochs, we looked to systems S1, S2, and S3 for time-variability. As shown in Figure 6, the Si IV trough depth becomes increasingly shallower over time, which may be explained by the same ionization effects that affect the S4 C IV BAL shown in Figure 5, discussed by Xu et al. (2020c). As the ionization parameter $U_{\rm H}$ changes, ions of particular ionization states become more or less abundant over time. Because the C IV of S4, along with the Si IV of S1, S2, and S3, decreases monotonically, this supports the assertion that the changes in the troughs are due to changes in the ionization parameter. Further observation and analysis will be required to confirm these effects.

5.3. SED and Metallicity Dependency, and Attenuation of the SED

An alternative to using the SED of HE0238 would be to use the theoretical SED as defined by Mathews & Ferland (1987), which is based on the He II line. The HE0238 SED is based on observation of a high-quality spectrum that stretches into the far-UV range, better representing a quasar spectrum (Arav et al. 2013). Just like in other objects (e.g., Xu et al. 2018; Miller et al. 2020a), higher metallicity drops the values of the energetics parameters, for instance, raising the metallicity to four times solar metallicity, using abundance ratios from Ballero et al. (2008), changes the photoionization solution of S2 to $\log U_H = -1.5^{+0.3}_{-0.3}$, and $\log N_H = 20.5^{+0.4}_{-0.4}$[cm^{-2}], and lowering the mass flow rate and kinetic luminosity to $\dot{M} = 1300^{+600}_{-400}\,M_\odot\ {\rm yr}^{-1}$ and $\log \dot{E}_K = 45.13^{+0.17}_{-0.18}$[erg s^{-1}], respectively. Using the SED by Mathews & Ferland (1987) with solar metallicity changes the solution to $\log U_H = -1.5^{+0.4}_{-0.4}$, $\log N_H = 21.2^{+0.5}_{-0.5}$, which is in agreement with the values in Table 3 within error.

It is possible that the SED seen by one outflow system can be attenuated by another, resulting in a smaller $Q_{\rm H}$ and, by extension, a smaller distance R. In particular, as S2 is farther out than the other mini-BAL system S3, it is likely that the SED seen by S2 is obscured by S3 (e.g., Bautista et al. 2010; Sun et al. 2017; Miller et al. 2018, 2020c). We used the method described by Miller et al. (2018) to test the effects of attenuation by S3. We used Cloudy to model the attenuated SED by S3 by inputting the relevant $N_{\rm H}$ and $U_{\rm H}$ values of S3 shown in Table 3. We then use that attenuated SED to find the resulting $Q_{\rm H}$ and R of S2. The reduced values for the parameters are $Q_{\rm H} = 4.9^{+0.5}_{-0.5} \times 10^{56}{\rm s}^{-1}$ and $R = 43^{+35}_{-20}$ kpc, which is a ∼30% decrease in the distance of S2. We choose S3 as the attenuation source, as its stronger features compared to S1 suggest that the attenuation effect from S3 would be larger than that of S1. We are unable to calculate the attenuation by S4, as we cannot obtain $N_{\rm H}$ or $U_{\rm H}$ from its singular C IV absorption trough.

5.4. Comparison with Other Outflows

There have been several prior studies of quasar outflow acceleration, including that of the acceleration of the outflow of quasar SDSS J1042+1646 conducted by Xu et al. (2020c), based on the acceleration seen in Ne VIII λλ770, 780. The bolometric luminosity of SDSS J1042+1646 is estimated to be $\sim 1.5 \times 10^{47}$ erg s^{-1}, which is comparable to that of J0242+0049 (1.9×10^{47} erg s^{-1}). The average acceleration of S4 that we have found ($a \approx -0.25$ cm s^{-2}) is roughly an order of magnitude smaller than that by Xu et al. (2020c; $a = -1.52$ cm s^{-2}), which suggests that if S4 is truly accelerating, the acceleration of quasar outflows can cover a wide range.

To give context to the study of outflow S2, we review a few outflows with a similarly large R and/or $\dot{E}_K$. Analysis of a molecular outflow of quasar SDSS J1148+5251 at a distance $R \sim 15$ kpc conducted by Maiolino et al. (2012) revealed a lower limit to the mass flow rate of $\dot{M} > 3500\,M_\odot\ {\rm yr}^{-1}$ as well as one for the kinetic luminosity $\dot{E}_K > 1.9 \times 10^{45}$erg s^{-1}.

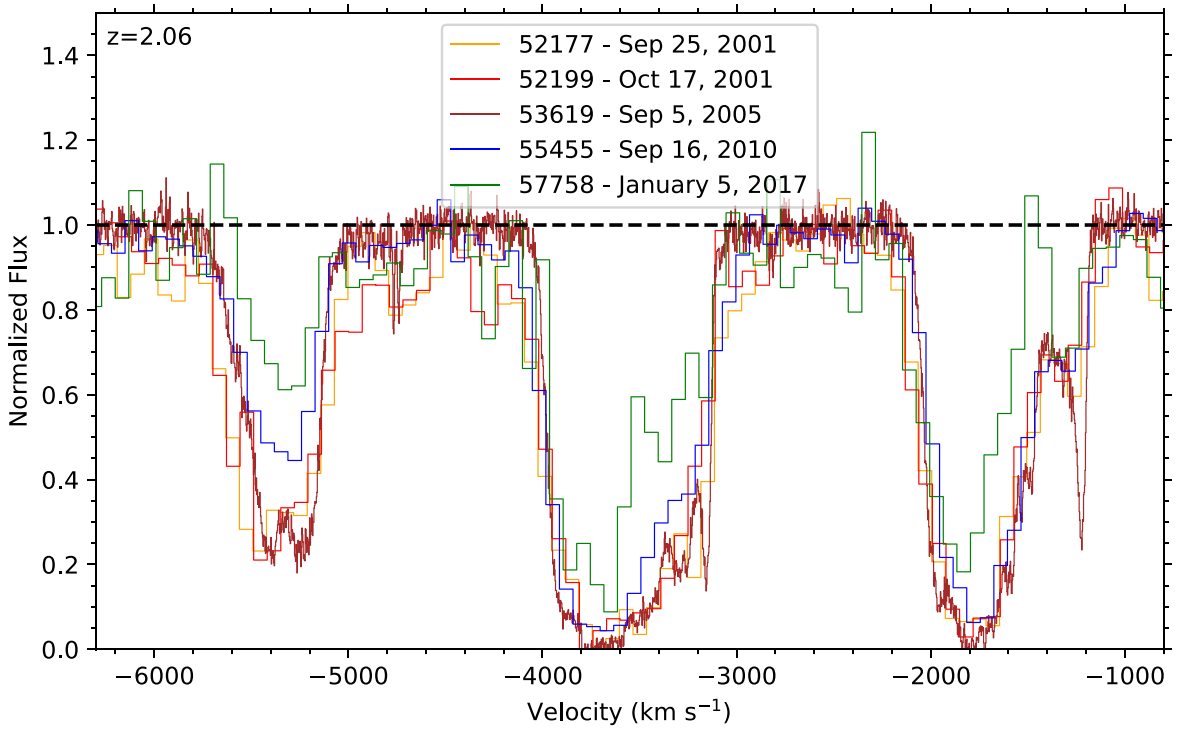

Figure 6. Normalized flux vs. velocity of Si IV troughs at different epochs. Note that the depth of the troughs becomes shallower over time.

Table 4
Velocities of C IV BAL at Each Epoch

MJD	Date	$\Delta t_{\rm Rest}$ (days)	v_n (km s^{-1})	Δv_n (km s^{-1})	EW$_n$ (km s^{-1})	v_w (km s^{-1})	Δv_w (km s^{-1})	EW$_w$ (km s^{-1})
52177	2001 Sep 25	0	−17,460 ± 50	0	1190	−19,000	0	1010
52199	2001 Oct 17	13.0	−17,600 ± 40	−140 ± 70	1320	−19,000	0	2140
53619	2005 Sep 5	838.6	−17,720 ± 4	−260 ± 50	920	−20,000	−1000	20
55455	2010 Sep 16	1922.8	−17,870 ± 40	−400 ± 60	460	−19,490	−490	860
57758	2017 Jan 5	3282.7	−18,180 ± 380	−720 ± 380	80	−19,000	0	260

Notes. Table of the centroid velocity and equivalent width of the C IV BAL for each epoch. $\Delta t_{\rm Rest}$ is the elapsed time in the quasar's rest frame since the 52177 epoch. v_n and v_w are the centroid velocities of the narrow and wide best-fit Gaussians in the quasar's rest frame, while Δv_n and Δv_w are the velocity shifts compared to those of the 52177 epoch. The equivalent widths (EW$_n$, EW$_w$) have been calculated by integrating over the Gaussians in velocity space. The parameters for the wider Gaussians are more affected by the continuum models for each epoch. Note that the uncertainty in the centroid velocity of the MJD = 53619 epoch is significantly smaller than those of the other epochs, due to the higher signal-to-noise ratio and resolution of the data.

Liu et al. (2013) analyzed the ionized gas around 11 radio-quiet quasars via the [O III] λ5007Å emission. These outflows were found between ∼10−20kpc from the central source, had velocities of up to −1000 km s^{-1}, and had an estimated $n_e \sim 1.2$ cm^{-3}. The outflows had an estimated range of $\dot{E}_K$ from 4×10^{44} to 3×10^{45} erg s^{-1}, and $\dot{M}$ from 2×10^3 to 2×10^4 $M_\odot$ yr^{-1}. These numbers are within a factor of a few of the values we find for S1, S2, and S3 (see Table 3), which suggests we may find similar outflows in absorption.

In their analysis of SDSS J1051+1247, Miller et al. (2020a) found an outflow system with $\dot{E}_K = 3 \times 10^{45}$erg s^{-1}. The mass flow rate ($\dot{M} = 6500\, M_\odot$ yr^{-1}) and kinetic luminosity ($\dot{E}_K = 6.6 \times 10^{45}$erg s^{-1}) of S2 align with these values and those of the objects mentioned above, within a margin of error. Xu et al. (2020a) claim the most energetic quasar outflow measurement to date from quasar SDSS J1042+1646 ($\dot{E}_K = 5 \times 10^{46}$erg s^{-1}), and this claim remains uncontested.

While the distance of S2 from the quasar is unprecedentedly large, there exists a theoretical model that may be supported by this observation. Faucher-Giguère et al. (2012) provide an argument that FeLoBALs, absorption systems with signs of Fe II, may be formed in situ at distances of several kiloparsecs. They clarify that while their model focuses on the formation of FeLoBALs at large distances, other classes of outflows may form as described by it.

6. Summary and Conclusion

This paper has presented the analysis of three absorption systems of quasar SDSS J0242+0049, dubbed S1, S2, and S3, from VLT/UVES observational data, as well as the velocity shift of the S4 C IV BAL across five different epochs. From the absorption troughs we identified, we measured the column densities of 11 ions in each system as shown in Table 2. Through photoionization analysis using the measured column densities, we found the best-fit solutions to $U_{\rm H}$ and $N_{\rm H}$ for each system.

The abundance ratios between the excited and resonance states of ions Si II and C II were used to find the electron number density n_e of the three systems S1, S2, and S3, as shown in Figure 4. Equations (5), (6), and (7) were used to find the distance from the central source, the mass flow rate, and the kinetic luminosity of each system respectively. The ratios between the kinetic luminosities and the quasar's Eddington luminosity were found in order to evaluate their AGN feedback contribution, the results of which can be seen in Table 3. From this analysis, we have found that S2 and S3 have sufficient kinetic luminosity for AGN feedback contribution. Most notable in this result is the distance of S2 $R = 67$ kpc, farther than the absorption system of 3C 191 found at $R = 28$ kpc by Hamann et al. (2001), making this the farthest reported distance of a mini-BAL absorption outflow from its central source.

Following the analysis of the three systems, we examined the change in velocity and equivalent width of the S4 C IV BAL, as shown in Figure 5, based on the UVES spectrum, as well as different SDSS observations. As seen in Table 4, there has been a monotonic increase in the line-of sight velocity, as well as a decrease in equivalent width, with the trough being a factor of 6 weaker at the epoch of 2017 January compared to that of 2001 September.

Through further observation and analysis, we expect to shed more light on the time-variability of the S4 C IV BAL, as well as that of systems S1, S2, and S3.

N.A. and D.B. acknowledge support from NSF grant No. AST 2106249, as well as NASA STScI grant Nos. GO 14777, 14242, 14054, 14176, and AR-15786. D.B. acknowledges support from the Virginia Space Grant Consortium Graduate Research Fellowship Program (award number 200009-010).

ORCID iDs

Doyee Byun https://orcid.org/0000-0002-3687-6552
Nahum Arav https://orcid.org/0000-0003-2991-4618
Patrick B. Hall https://orcid.org/0000-0002-1763-5825

References

Abbott, D. C. 1982, ApJ, 259, 282
Allen, J. T., Hewett, P. C., Maddox, N., Richards, G. T., & Belokurov, V. 2011, MNRAS, 410, 860
Arav, N., Becker, R. H., Laurent-Muehleisen, S. A., et al. 1999a, ApJ, 524, 566
Arav, N., Borguet, B., Chamberlain, C., Edmonds, D., & Danforth, C. 2013, MNRAS, 436, 3286
Arav, N., Kaastra, J., Kriss, G. A., et al. 2005, ApJ, 620, 665
Arav, N., Korista, K. T., de Kool, M., Junkkarinen, V. T., & Begelman, M. C. 1999b, ApJ, 516, 27
Arav, N., & Li, Z.-Y. 1994, ApJ, 427, 700
Arav, N., Liu, G., Xu, X., et al. 2018, ApJ, 857, 60
Arav, N., Xu, X., Miller, T., Kriss, G. A., & Plesha, R. 2020, ApJS, 247, 37
Astropy Collaboration, Robitaille, T. P., Tollerud, E. J., et al. 2013, A&A, 558, A33
Astropy Collaboration, Price-Whelan, A. M., Sipőcz, B. M., et al. 2018, AJ, 156, 123
Bahk, H., Woo, J.-H., & Park, D. 2019, ApJ, 875, 50
Ballero, S. K., Matteucci, F., Ciotti, L., Calura, F., & Padovani, P. 2008, A&A, 478, 335
Barlow, T. A., Hamann, F., & Sargent, W. L. W. 1997, in ASP Conf. Ser. 128, Mass Ejection from Active Galactic Nuclei, ed. N. Arav, I. Shlosman, & R. J. Weymann (San Francisco, CA: ASP), 13
Bautista, M. A., Dunn, J. P., Arav, N., et al. 2010, ApJ, 713, 25
Bennett, C. L., Larson, D., Weiland, J. L., & Hinshaw, G. 2014, ApJ, 794, 135
Borguet, B., Edmonds, D., Arav, N., Dunn, J., & Kriss, G. A. 2012, ApJ, 751, 107
Borguet, B. C. J., Edmonds, D., Arav, N., Benn, C., & Chamberlain, C. 2012a, ApJ, 758, 69
Borguet, B. C. J., Edmonds, D., Arav, N., Dunn, J., & Kriss, G. A. 2012b, ApJ, 751, 107
Chamberlain, C., Arav, N., & Benn, C. 2015, MNRAS, 450, 1085
Chen, C., Hamann, F., Ma, B., & Murphy, M. 2021, ApJ, 907, 84
Ciotti, L., Ostriker, J. P., & Proga, D. 2009, ApJ, 699, 89
Dai, X., Shankar, F., & Sivakoff, G. R. 2008, ApJ, 672, 108
de Kool, M., Arav, N., Becker, R. H., et al. 2001, ApJ, 548, 609
de Kool, M., Becker, R. H., Gregg, M. D., White, R. L., & Arav, N. 2002, ApJ, 567, 58
de Kool, M., Korista, K. T., & Arav, N. 2002, ApJ, 580, 54
Dere, K. P., Landi, E., Mason, H. E., Monsignori Fossi, B. C., & Young, P. R. 1997, A&AS, 125, 149
Dere, K. P., Zanna, G. D., Young, P. R., Landi, E., & Sutherland, R. S. 2019, ApJS, 241, 22
Dunn, J. P., Bautista, M., Arav, N., et al. 2010, ApJ, 709, 611
Edmonds, D., Borguet, B., Arav, N., et al. 2011, ApJ, 739, 7
Faucher-Giguère, C.-A., Quataert, E., & Murray, N. 2012, MNRAS, 420, 1347
Ferland, G. J., Chatzikos, M., Guzmán, F., et al. 2017, RMxAA, 53, 385
Gabel, J. R., Arav, N., & Kim, T.-S. 2006, ApJ, 646, 742
Gabel, J. R., Kraemer, S. B., Crenshaw, D. M., et al. 2005, ApJ, 631, 741
Hall, P. B., Sadavoy, S. I., Hutsemekers, D., Everett, J. E., & Rafiee, A. 2007, ApJ, 665, 174
Hamann, F., & Sabra, B. 2004, in ASP Conf. Ser. 311, AGN Physics with the Sloan Digital Sky Survey, ed. G. T. Richards & P. B. Hall (San Francisco, CA: ASP), 203
Hamann, F. W., Barlow, T. A., Chaffee, F. C., Foltz, C. B., & Weymann, R. J. 2001, ApJ, 550, 142
Hewett, P. C., & Foltz, C. B. 2003, AJ, 125, 1784
Hopkins, P. F., & Elvis, M. 2010, MNRAS, 401, 7
Knigge, C., Scaringi, S., Goad, M. R., & Cottis, C. E. 2008, MNRAS, 386, 1426
Liu, G., Zakamska, N. L., Greene, J. E., Nesvadba, N. P. H., & Liu, X. 2013, MNRAS, 436, 2576
Lucy, L. B., & Abbott, D. C. 1993, ApJ, 405, 738
Maiolino, R., Gallerani, S., Neri, R., et al. 2012, MNRAS, 425, L66
Mathews, W. G., & Ferland, G. J. 1987, ApJ, 323, 456
Miller, T. R., Arav, N., Xu, X., Kriss, G. A., & Plesha, R. J. 2020a, ApJS, 247, 39
Miller, T. R., Arav, N., Xu, X., Kriss, G. A., & Plesha, R. J. 2020b, ApJS, 249, 15
Miller, T. R., Arav, N., Xu, X., Kriss, G. A., & Plesha, R. J. 2020c, ApJS, 247, 41
Miller, T. R., Arav, N., Xu, X., et al. 2018, ApJ, 865, 90
Moe, M., Arav, N., Bautista, M. A., & Korista, K. T. 2009, ApJ, 706, 525
Murphy, M. T., Kacprzak, G. G., Savorgnan, G. A., & Carswell, R. F. 2019, MNRAS, 482, 3458
Osterbrock, D. E., & Ferland, G. J. 2006, Astrophysics of Gaseous Nebulae and Active Galactic Nuclei (Sausalito, CA: University Science)
Pâris, I., Petitjean, P., Aubourg, É., et al. 2018, A&A, 613, A51
Richards, G. T., Lacy, M., Storrie-Lombardi, L. J., et al. 2006, ApJS, 166, 470
Savage, B. D., & Sembach, K. R. 1991, ApJ, 379, 245
Scannapieco, E., & Oh, S. P. 2004, ApJ, 608, 62
Schlafly, E. F., & Finkbeiner, D. P. 2011, ApJ, 737, 103
Schneider, D. P., Richards, G. T., Hall, P. B., et al. 2010, AJ, 139, 2360
Silk, J., & Rees, M. J. 1998, A&A, 331, L1
Smee, S. A., Gunn, J. E., Uomoto, A., et al. 2013, AJ, 146, 32
Sun, L., Zhou, H., Ji, T., et al. 2017, ApJ, 838, 88
Tsuzuki, Y., Kawara, K., Yoshii, Y., et al. 2006, ApJ, 650, 57
Vayner, A., Wright, S. A., Murray, N., et al. 2021, ApJ, 919, 122
Weymann, R. J., Morris, S. L., Foltz, C. B., & Hewett, P. C. 1991, ApJ, 373, 23
Woo, J.-H., Le, H. A. N., Karouzos, M., et al. 2018, ApJ, 859, 138
Xu, X., Arav, N., Miller, T., & Benn, C. 2018, ApJ, 858, 39
Xu, X., Arav, N., Miller, T., & Benn, C. 2019, ApJ, 876, 105
Xu, X., Arav, N., Miller, T., Kriss, G. A., & Plesha, R. 2020a, ApJS, 247, 38
Xu, X., Arav, N., Miller, T., Kriss, G. A., & Plesha, R. 2020b, ApJS, 247, 42
Xu, X., Arav, N., Miller, T., Kriss, G. A., & Plesha, R. 2020c, ApJS, 247, 40
Yuan, F., Yoon, D., Li, Y.-P., et al. 2018, ApJ, 857, 121